ARMY RESEARCH LABORATORY

Prediction of Electromagnetic Fields Generated by Rail Guns

by Ira Kohlberg

ARL-CR-148

September 1995

prepared by

Kohlberg Associates, Inc.
5375 Duke Street, Unit 1603
Alexandria, VA 22304

under contract

DAAL03-91-C-0034
Subcontract 93419

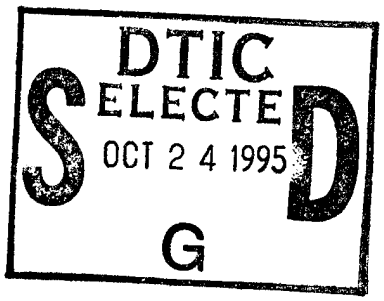

The findings in this report are not to be construed as an official Department of the Army position unless so designated by other authorized documents.

Citation of manufacturer's or trade names does not constitute an official endorsement or approval of the use thereof.

Destroy this report when it is no longer needed. Do not return it to the originator.

REPORT DOCUMENTATION PAGE

Form Approved
OMB No. 0704-0188

1. AGENCY USE ONLY *(Leave blank)*	2. REPORT DATE	3. REPORT TYPE AND DATES COVERED
	September 1995	Final, from Jul 93 to Jan 94

4. TITLE AND SUBTITLE
Prediction of Electromagnetic Fields Generated by Rail Guns

5. FUNDING NUMBERS
PE: 61102A

6. AUTHOR(S)
Ira Kohlberg
ARL POC: William O. Coburn

7. PERFORMING ORGANIZATION NAME(S) AND ADDRESS(ES)
Kohlberg Associates, Inc.
5375 Duke Street, Unit 1603
Alexandria, VA 22304

8. PERFORMING ORGANIZATION REPORT NUMBER
ARL-CR-148

9. SPONSORING/MONITORING AGENCY NAME(S) AND ADDRESS(ES)
U.S. Army Research Laboratory
Attn: AMSRL-WT-ND
2800 Powder Mill Road
Adelphi, MD 20783-1197

10. SPONSORING/MONITORING AGENCY REPORT NUMBER

11. SUPPLEMENTARY NOTES
AMS code: P611102.00000
ARL PR: 3E25E3
Contract No.: DAAL03-91-C-0034
Subcontract No.: 93419

12a. DISTRIBUTION/AVAILABILITY STATEMENT
Approved for public release; distribution unlimited.

12b. DISTRIBUTION CODE

13. ABSTRACT *(Maximum 200 words)*

Electromagnetic launch systems such as rail guns generate electromagnetic signatures that contain a spectrum of frequencies extending from quasi-DC up to tens of kilohertz. However, electromagnetic compatibility (EMC) considerations pertaining to the potential adverse effects of these fields on nearby electronic equipment remain largely unexplored. This report includes a discussion of the theoretical models used to predict the inductance gradient, the transient behavior of the currents produced in the rail gun structure, the dynamical generation of the external fields, and a comparison of the theoretical model with experimental data.

The predicted rail inductance gradient of $L'_R = 0.52$ μH/m compares very well with the measured value of 0.522 μH/m. The existence of an inductance gradient efficiency factor, E_0, is demonstrated, with a derived value of 0.75. This produces an effective inductance gradient of $L' = E_0 L'_R = 0.39$ μH/m. Using this value of L' leads to a theoretical exit muzzle velocity of 525 m/s, which is within 5 percent of the measured value.

14. SUBJECT TERMS	15. NUMBER OF PAGES
Rail gun, EM fields, magnetic field	42
	16. PRICE CODE

17. SECURITY CLASSIFICATION OF REPORT	18. SECURITY CLASSIFICATION OF THIS PAGE	19. SECURITY CLASSIFICATION OF ABSTRACT	20. LIMITATION OF ABSTRACT
Unclassified	Unclassified	Unclassified	UL

13. ABSTRACT (cont'd)

The predicted waveshapes of the magnetic field components are generally in good agreement with observations for points close to the bore center. For radial distances greater than a foot, the experiments show peak fields that may exceed the predictions by a factor of two to three. These issues are being investigated.

Contents

Appendices

Figures

Tables

1. Introduction

In recent years significant advances have been made in the development of electromagnetic launchers (EMLs). These devices can impart hypervelocities to macroscopic size objects (e.g., greater than several grams). Possibilities even exist for launching aerospace platforms using this technology. A rail gun is a type of EML that shows promise of being implemented into operating systems in the near future. Figure 1 shows a generic model of a rail gun that is similar to the one used in our experiments.

A robust pulse power source (see sect. 2) provides a burst of energy lasting several milliseconds that drives the projectile between the rails; the projectile eventually leaves the system with a velocity in the kilometers per second range. The currents may exceed 10^5 A, and can generate very strong magnetic fields ($H > 10^4$ A/m) close to the rails, which drop off with distance from the rails. The dominant portion of the electromagnetic signatures contains frequencies from dc to tens of kilohertz. Depending on the physical contact between the projectile and rails, there may also be intermittent arcing at the contact surface. In addition, the emergence of the projectile from the rails is accompanied by arcing, which is alleviated by placing a resistive load across the muzzle.

As rail guns emerge from laboratory models toward implementation into systems, one must consider the electromagnetic compatibility (EMC) issues due to the electromagnetic fields generated by these devices from the enormous currents produced on the rails. The first step in assessing EMC problems is the characterization of these fields as a function of time and distance from the rails. This report describes the present status of our theoretical model used to predict these fields, as well as including a limited comparison with experimental data. Recent papers by Coburn et al [1,2] address the observations and experimental configuration in detail.

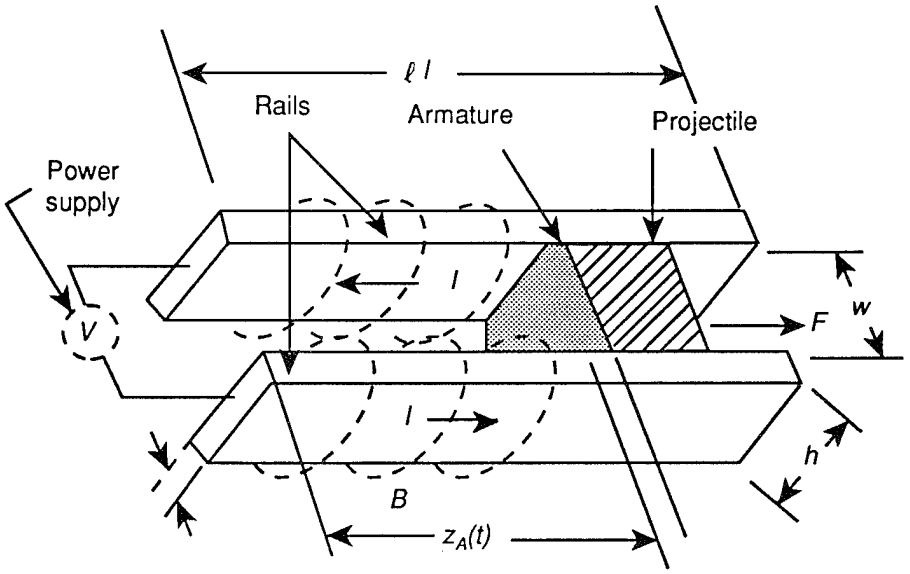

Figure 1. Rail gun and coordinate system.

The incorporation of a rail gun into a weapon system requires a quantification of the relationship between the power source, rail gun dynamics, and electromagnetic fields generated by the rail and armature currents. In order to ensure EMC with other equipment it is necessary to characterize not only the dominant low-frequency (dc to tens of kilohertz) fields generated by the moving armature, but also the higher frequency emissions generated by continuum arcing along the rails, and the larger arc produced at the muzzle. For predicting the low-frequency magnetic fields, the circuit approximation to the rails, which has traditionally been used to study armature acceleration, appears to be adequate. On the other hand, a modal analysis of the rail system model viewed as a transmission line is required at the higher frequencies in order to model arcing contributions. In addition, it may be necessary to incorporate the effects of electromagnetic shielding in the evaluation of EMC for an actual system.

This report is the first in a series of reports that eventually will provide the ability to quantify EMC considerations for all frequencies of interest. We concentrate at present only on the low-frequency magnetic field generated by the rail current in a solid armature, for which there is negligible arcing. It includes a discussion of the pulsed power source, theoretical considerations for predicting the fields, and a comparison between theory and experiment.

2. Electromagnetic Model for Rail Gun

Figure 2 shows a circuit model for the rail gun that includes a circuit diagram for the pulsed power system. The rails are connected to four capacitor banks, each composed of a 2000-μF capacitor and a 12-μH inductor. Diodes are placed across the capacitor bank to prevent reverse current. The charging voltage is typically 4 kV. The circuit includes the ohmic resistance and inductance of the source and the connection to the rails. The 100-Ω load resistor serves as a means to measure the muzzle voltage.

The time behavior of the current is determined by combining the circuit model of figure 2 with the equations for the motion of the armature. It can be shown that to a good approximation the rail system can be modelled as a lossless transmission line with inductance and capacitance per unit length defined as L_R' and C_R', respectively. C_R' is related to L_R' by the equation

$$C_R' = (\varepsilon_0 \mu_0)/L_R' \quad , \tag{1}$$

and for our application is shown to be negligible. Thus, capacitive effects are not important.

The power supplied to the rails, $V_0 I_0$, is given by

$$V_0 I_0 = \frac{1}{2}\frac{d}{dt}\left[Z_A L_R' I_0^2\right] + V_L I_0 \quad , \tag{2}$$

where the first term on the right-hand side is the magnetic energy increase per unit time, and the second term, $V_L I_0$, is the power supplied to the armature. Closure for the system of equations is completed by relating the armature position Z_A, and the power supplied to it, to the current. The canonical equation for the armature acceleration is

$$m\frac{d^2 Z_A}{dt^2} = F_z = \frac{1}{2} L_e' I_0^2 \quad , \tag{3}$$

where m is the mass of the projectile plus armature, and L_e' is an *effective* inductance per unit length. The selection of the appropriate value of L_e' has been of longstanding interest in rail gun theory. A commonly used

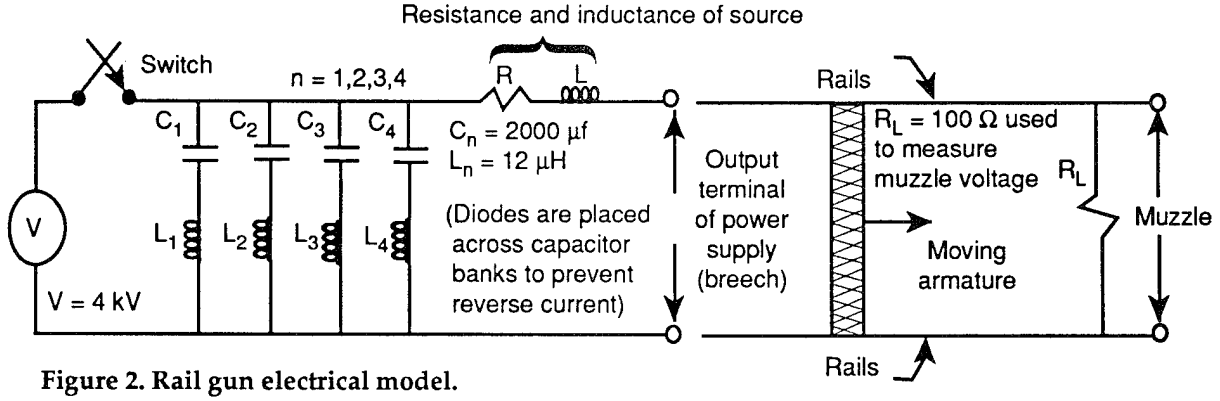

Figure 2. Rail gun electrical model.

value was L'_R; this, however, frequently led to results that were at variance with experiment. In this report we show that L'_e can be written as

$$L'_e = E_0 L'_R \ , \tag{4}$$

where E_0 is an electromagnetic efficiency factor that is always less than unity.

When the correct value of L'_e is used, the velocity, $\dot{Z}_A$, is

$$\dot{Z}_A = \left(\frac{L'_e}{2m}\right) \int_0^t I_0^2(t')\, dt' \ . \tag{5}$$

Since the electrical power supplied to the mass, $V_L I_0$, must equal its rate of increase in kinetic energy, we have

$$V_L I_0 = F_z \dot{Z}_A \ . \tag{6}$$

Equations (2) to (6), when combined with the circuit model for the power source, determine the current, voltage, and armature position.

As we show in section 4, L'_e is determined from a two-step process. The first part is the evaluation of the inductance per unit length, L'_R, for the rails viewed as a parallel plate transmission line. The second part deals with the realization that only a fraction of L'_R, which we call the efficiency factor, E_0, is actually involved in the armature acceleration process. This leads to the derivation of equation (4).

The electromagnetic theory [3–7] that leads to the derivation of L'_R and E_0 also uniquely determines the electric and magnetic fields, and rail surface currents in the x-y plane (sect. 4.2). Strictly speaking, the surface currents are *never* uniformly distributed along the rail surfaces, although a uniform surface current assumption may be acceptable when the ratio of rail height-to-separation, a/b, is large (see fig. 6, p 11).

For characteristic distances from the rail center, D_0, that are much greater than both a or b, the detailed distribution of surface currents along the rails is immaterial to the value of the magnetic field. In this case the approximation of the rails as current filaments is entirely adequate; the filament approximation then also applies to the armature. Table 1 summarizes the choice of electromagnetic field model as a function of D_0 compared with a and b. For the uniform sheet and filament models, the magnetic fields are determined by a straightfoward application of the Biot-Savart law. Since experimental observation has been made only in the regions where $D_0 > a, b$, we discuss the analytical results for these models in section 6.

Table 1. EM model as function of D_0.

D_0	EM model
$D_0 \sim b, a$	Conformal mapping
$D_0 > b, a,$	Uniform sheet (when $a > b$)
$D_0 >> b, a$	Filament

3. Inductance and Shielding Considerations

This section addresses certain EMC issues that are important in the integration of rail guns into larger systems. Two basic requirements are involved here: (1) that the introduction of the rail gun does not adversely affect the performance of other systems and (2) that the rail gun power efficiency be acceptable. This latter requirement means that for a given power source, a significant fraction of the pulse energy be transferred to the projectile as compared with increasing the magnetic field energy around the rails.

Figure 3 shows a model of the rail gun in the support structure used in our experiments. No special attempt was made to shield the magnetic fields. If, however, a structure of this type were to be used to shield nearby electronic equipment, the external frame would have a relative permeability, μ_r, greater than unity. In this case, not only would the rail inductance gradient be changed from L_R' to a new value, but also the electromagnetic efficiency would be changed. Theoretical predictions for this case have not yet been made. The essential challenge for EMC is to achieve the desired balance between rail gun energy efficiency and shielding.

On the other hand, it is possible to estimate the amount of shielding required by approximating the rails as current filaments encased in a cylindrical shell of thickness $\Delta = r_2 - r_1$, as shown in figure 4. The solution for the fields has been worked out by Smythe [8]. The magnetic vector potential has only one component, $A_z(z,t)$ that is given by

$$A_z = \frac{4\mu_0 I}{\pi} \sum_{n=0}^{\infty} \left[(\mu_r+1)^2 - (\mu_r-1)^2 \left(\frac{r_1}{r_2}\right)^{4n+2} \right]^{-1} \frac{1}{2n+1} \left(\frac{w}{2r}\right)^{2n+1} \cos(2n+1)\theta \ , \quad (7)$$

where μ_r is the relative permeability, and the current, I, is a function of time determined from the solution of the equations in section 2. The magnetic field components in cylindrical coordinates are given by

$$B_r = \frac{1}{r} \frac{\partial A_z}{\partial \theta} \ , \quad B_\theta = \frac{\partial A_z}{\partial r} \ . \quad (8)$$

Figure 3. Rail gun in support structure.

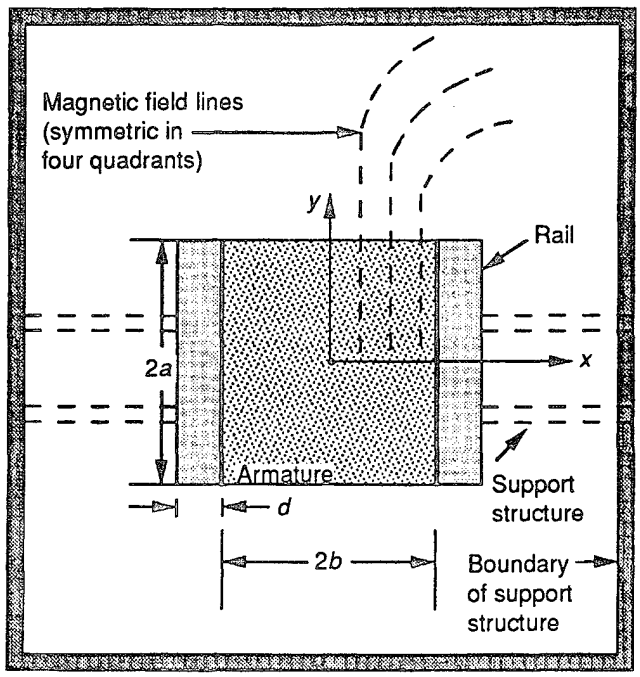

Figure 4. Model for estimating magnetic shielding.

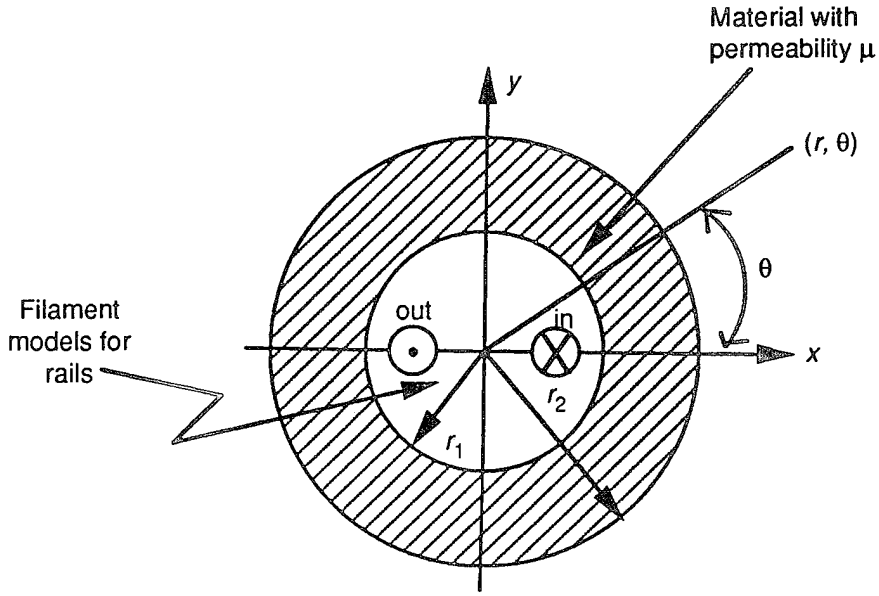

4. Physical Models

4.1 Force on Armature and Equations of Motions

Figure 5 shows the top view of the rail gun, while figure 6 shows a blow-up of the armature relevant to the calculation of the accelerating force in the z-direction. As indicated, figure 6 is rotated 90° counterclockwise from figure 5 to make the coordinate system compatible with the conformal mapping discussion of section 4.2. We have also indicated the existence of surface currents in figure 5 that are assumed to penetrate into the conducting surfaces. They do not, however, affect the derivation of the armature force, F_a.

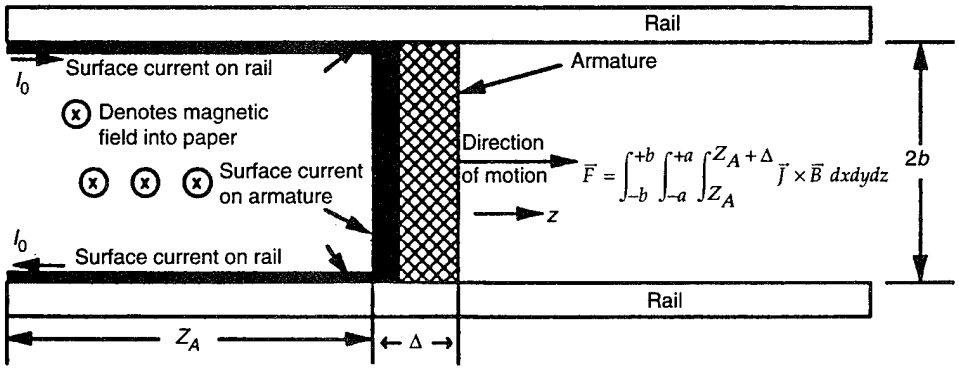

Figure 5. Top view of rail gun.

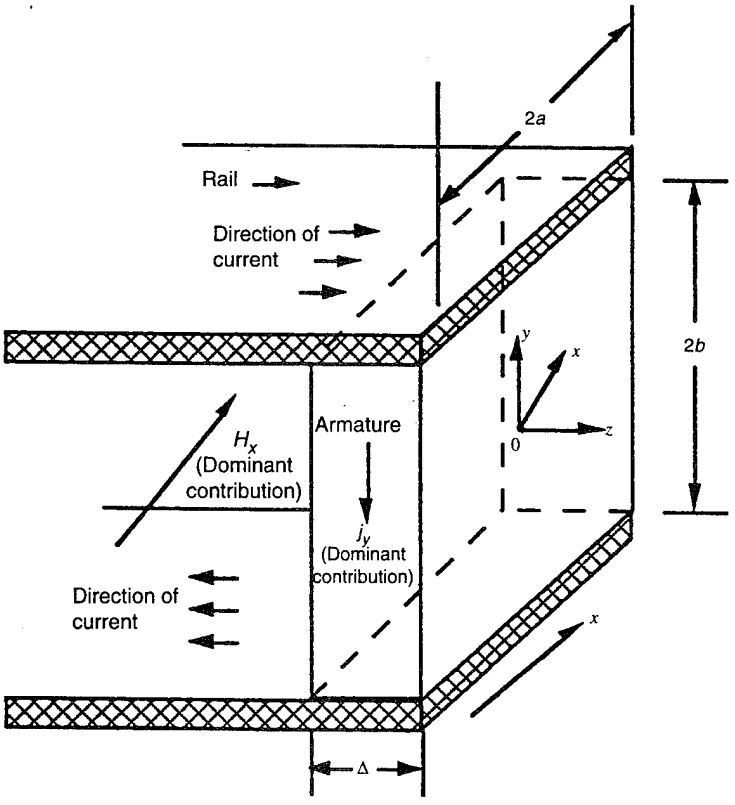

Figure 6. Computation of force on armature.

F_a is determined by initially formulating the force per unit volume in the armature $\vec{f}_v$ and then integrating over the armature volume. The volumetric force is given by

$$\vec{f}_v = \vec{j} \times \vec{B} \ , \tag{9}$$

where $\vec{j}$ is the current density and $\vec{B} = \mu_0 \vec{H}$ is the magnetic flux density. From Maxwell's equations we have the relationship

$$\vec{j} = \nabla \times \vec{H} \ . \tag{10}$$

Using equation (10) in equation (9) then gives the total force,

$$\vec{F} = \mu_0 \int_{-b}^{+b} \int_{-a}^{+a} \int_{Z_A}^{Z_A + \Delta} (\nabla \times \vec{H}) \times \vec{H} \ dx \, dy \, dz \ . \tag{11}$$

Application of the vector identity

$$(\vec{H} \cdot \nabla) \vec{H} = \frac{1}{2} \nabla (H^2) - \vec{H} \times (\nabla \times \vec{H}) \tag{12}$$

converts the volume integral into a surface integral. The z-component of $\vec{F}$ is the acceleration force, $F_a = F_z$, and is given by

$$F_z = \mu_0 \int_S H_z \vec{H} \cdot d\vec{S} + \frac{\mu_0}{2} \int_{-b}^{+b} \int_{-a}^{+a} \left[H^2(z = Z_A) - H^2(z = Z_A + \Delta) \right] dx \, dy \ . \tag{13}$$

The first term in equation (13) is a surface integral over all the six surfaces of the armature shown in figure 6. For a good conductor, the components of $\vec{H}$ normal to the armature surfaces will be very small, and the first term in equation (13) will then be negligible compared to the second.

If we assume that $H^2(z = Z_A + \Delta) << H^2 \ (z = Z_A)$, which is consistent with the generally assumed notion that there is only a minimal magnetic field in front of the armature, the accelerating force becomes

$$F_z = \frac{\mu_0}{2} \int_{-b}^{+b} \int_{-a}^{+a} H^2(z = Z_A) \ dx \, dy \ . \tag{14}$$

In the next section we show that

$$F_z = \frac{1}{2} E_0 L'_R I^2 \ , \tag{15}$$

where E_0 is the previously defined efficiency factor. The armature acceleration is then determined from the equation

$$m_A \frac{d^2 Z_A}{dt^2} = \frac{1}{2} E_0 L'_R I^2 \ , \tag{16}$$

and the power supplied to the armature is $F_z(dZ_A/dt)$.

4.2 Rail Gun Viewed as Transmission Line: Driving Inductance Per Unit Length

The purpose of this section is to derive equation (15) using the techniques of conformal mapping. Accurate evaluation of L'_R is available from C. E. Baum et al [6]. Although a rigorous determination of E_0 is still in progress (see app A), we present an estimate of this parameter based on an early investigation presented by Assadourian and Rimai [3].

Figure 7 shows the rail gun viewed as a transmission line. The inductance per unit length, L'_R, and the rail capacitance per unit length, C'_R, are determined from the solution of Maxwell's equations for the transverse electromagnetic (TEM) mode. It is this mode that applies when transmission line theory is used. The circuit model for the rail gun is itself the limiting form of the transmission line version of the rail gun system applied at zero frequency.

The TEM mode may alternatively be viewed as a quasi-static solution to the class of field problems solved by Laplace's equation in two dimensions:

$$\frac{\partial^2 V}{\partial x^2} + \frac{\partial^2 V}{\partial y^2} = 0 \ , \tag{17}$$

where V is the voltage. The capacitance per unit length for the rail gun system of figure 7 is found by first solving equation (17) for the boundary condition where the top conductor is at potential V_0 and the bottom conductor at potential $-V_0$. Surface charge density at each conductor, $\sigma_s(x, y)$, is determined from the equation

$$\sigma_s(x, y) = \varepsilon_0 E_n = -\varepsilon_0 (\nabla V)_n \ , \tag{18}$$

where E_n is the normal component of the electric field on the conducting surface, and the total charge per unit length, Q, on the top conductor is found by integrating equation (18) over the surface. A charge per unit length of $-Q$ resides on the bottom conductor in order to close the electric flux lines.

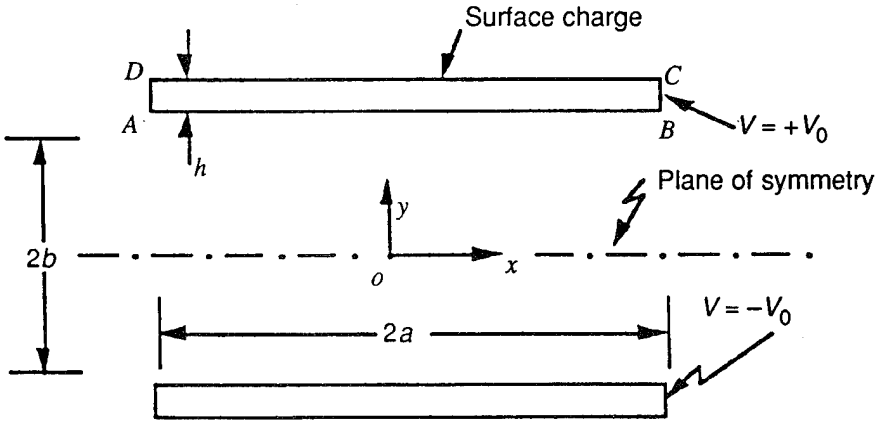

Figure 7. Transmission line model for rail gun.

It is important to note that surface charge will not only accrue on the inner surfaces facing one another, but also on the edges and on the top surface. In any event, the capacitance per unit length is then found from the formula

$$C'_R = \frac{Q}{2V_0} \ . \tag{19}$$

By expressing C'_R in the form [6]

$$C'_R = \varepsilon_0 / f_g \ , \tag{20}$$

where f_g is a geometric factor that depends only on the ratio, b/a, and then using the velocity of light, v_l,

$$v_l = \frac{1}{\sqrt{L'_R C'_R}} = \frac{1}{\sqrt{\varepsilon_0 \mu_0}} \ , \tag{21}$$

gives

$$L'_R = f_g \mu_0 \ . \tag{22}$$

Table 2 provides values of f_g as a function of (b/a) for a width-to-height ratio that may be of interest in rail guns. For the ARL rail gun, $(b/a) = 0.8$, which then gives $L'_R = (0.415)(4\pi \times 10^{-7}) = 0.52\ \mu H/m$. The method by which equation (17) is solved is that of conformal mapping [3–7], which has formed the basis for analytical solution of Laplace's equation in complex geometries such as the rail gun. Although the field problem is formulated as an electrostatic problem, from which the surface charge density, $\sigma_s(x, y)$, and the electrostatic field, $\vec{E}(x, y)$, in all x-y space is determined, the properties of the magnetic field and surface current distribution are also readily available. It is well known from TEM mode theory that if a total current I is flowing on a conductor, the spatial distribution of current density, $j_s(x, y)$, is

$$j_s(x, y) = \left(\frac{\sigma_s(x, y)}{Q}\right) I \ , \tag{23}$$

where $\sigma_s(x,y)$ and Q are computed for the corresponding electrostatic problem. As shown in appendix B, $\vec{H}(x, y)$ is given by

$$\vec{H} = \frac{I}{Q} \varepsilon_o \vec{k}_z \times \vec{E} \ , \tag{24}$$

where $\vec{k}_z$ is the unit vector in the z-direction.

The ratio, $\sigma_s(x, y)/Q$, is the normalized distribution of charge per unit length that satisfies the path integration, and

$$\frac{1}{Q} \oint_{ABCDA} \sigma_s(x, y)\, ds = 1 \ , \tag{25}$$

is a function only of b/a, and has dimensions of $(\text{length})^{-1}$. Since the electric field, $\vec{E}$, will also be proportional to the potential difference, $2V_o$, the ratio of $\vec{E}/Q$ will depend only on the geometry.

Table 2. f_g as function of b/a (selected results).

b/a	f_g	b/a	f_g
0.5	0.306	0.9	0.444
0.6	0.346	1.0	0.472
0.7	0.382	1.2	0.522
0.8	0.415	1.4	0.566

(Table source: Ref 6.)

In summary, the conformal mapping solution to Laplace's equation applied to the parallel plate rail gun uniquely determines the inductance per unit length, L'_R, the distribution of current on the rail surfaces, and the spatial distribution of the magnetic field. Figure 8 shows a sample of magnetic field lines in one quadrant of the geometry.

L'_R is defined by the standard equation

$$\frac{1}{2} L'_R I^2 = \frac{\mu_0}{2} \int_x \int_y H^2 \, dx \, dy \ , \tag{26}$$

where $\vec{H}$ lies in the x-y plane. The integration of equation (26) is carried out over the *entire* x-y plane, *not* just the surface of the armature. By combining equations (14) and (26) we derive the result

$$F_z = E_0 \frac{1}{2} L'_R I^2 \ , \tag{27}$$

where the efficiency factor, E_0, is given by

$$E_0 = \frac{\int_{-a}^{+a} \int_{-b}^{+b} H^2 \, dx \, dy}{\int_{-a}^{+a} \int_{-b}^{+b} H^2 \, dx \, dy + \int' \int' H^2 \, dx \, dy} \tag{28}$$

and $\int' \int'$ signifies the x-y integration external to the area of the armature; this is the leakage contribution.

It is possible to render an estimate of E_0 using an approximation developed by Assadourian and Rimai [3]. Their results, as expressed in our terminology, are rendered in figure 9. For the Army Research Laboratory (ARL) rail gun, $(2a/b) = 2.5$, which then gives an efficiency factor of about 75 percent. The appropriate inductance per unit length to use for acceleration is then $L'_e = E_0 L_R = (0.75)\ (0.52) = 0.39\ \mu H/m$. It will be shown in section 6 that the value of L'_e provides good agreement with experimental data.

Figure 8. Magnetic field lines in upper right-hand quadrant.

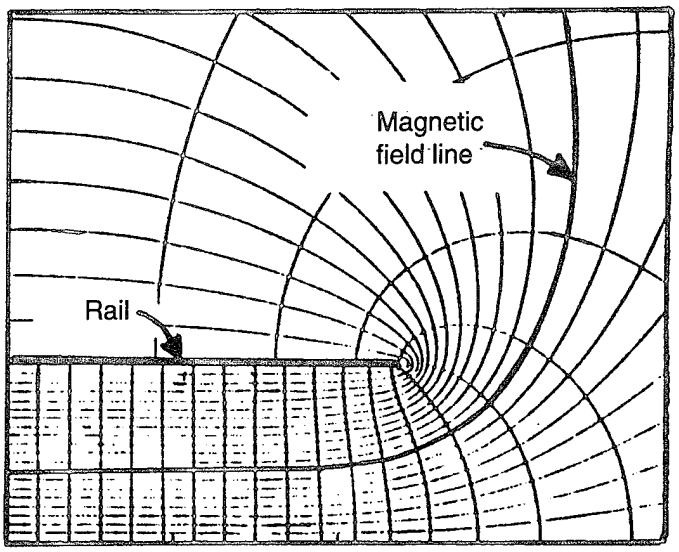

Figure 9. Inductance efficiency as a function of $2a/b$.

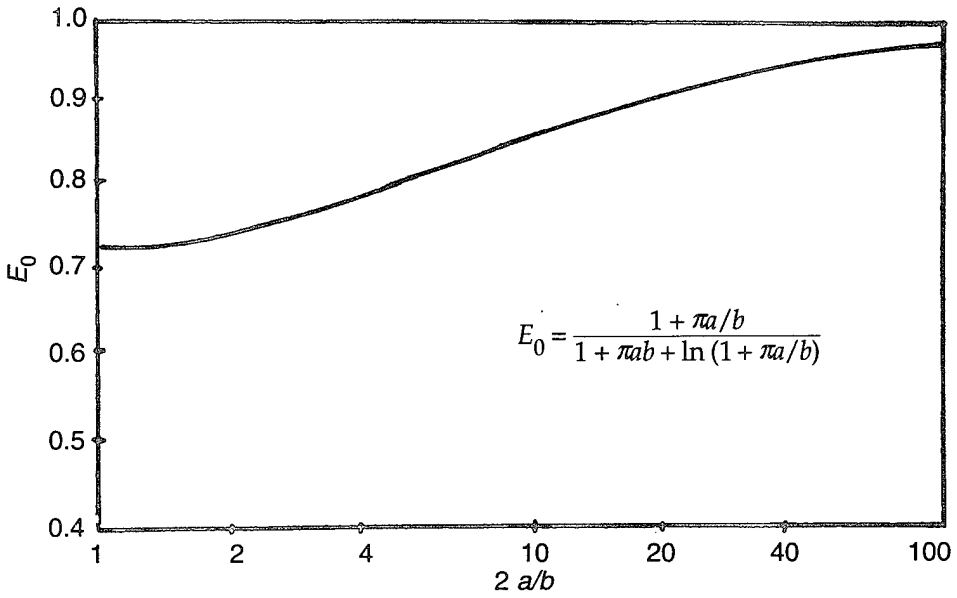

Source: Reference 3

5. Computation of Magnetic Fields

This section addresses the computation of the magnetic fields for the experimental configuration used in this study. In this case there is essentially no shielding introduced by the support structure for the rail gun system, and contributions to the electromagnetic fields arise from the currents flowing on the rails and armature. For each current source the Biot-Savart law can be used to compute the magnetic field, $\vec{H}$, since the wavelengths associated with the frequencies of interest are much larger than the characteristic dimensions of interest.

Figures 10 and 11 show the geometry for computing the contributions to the magnetic field intensity $\vec{H}$ from the armature and rails, respectively. If we assume in the general case that the current is distributed vertically, so that $J(y)\,dy$ is the differential current between y and $y + dy$, we have

$$d\vec{H} = \frac{Jdy}{4\pi}\int_S \frac{\vec{ds}\,x\vec{r}}{r^3}\ , \tag{29}$$

where $\vec{ds}$ is a differential vector pointing in the direction of the current, $\vec{r}$ is the distance from $\vec{ds}$ to the observation point whose coordinates are x, y, z, and r is the magnitude of $\vec{r}$. For the armature $\vec{ds} = dx\ \vec{i}$, where $\vec{i}$ is a unit vector in the x-direction, and for the rails $\vec{ds} = \pm dz\ \vec{k}$, where $\vec{k}$ is a unit vector in the z-direction. The "+" sign is used for the rail whose current is coming out of the paper, and the "–" sign for inward-directed current.

If $D = (X^2 + Y^2)^{1/2}$ is the transverse radial dimension of the field point, and D_0 is the maximum of either h or w, there arise two cases of practical interest. These are the situations where: (1) D is slightly greater than D_0, or (2) $D >> D_0$. In the former case the detailed structure of $J(y)$ may be important, while for case (2) the detailed structure of $J(y)$ is not important, and current filament approximations to the armature and rail currents may be used.

The distribution of surface current for the rails is determined from the conformal mapping solution for the inductance per unit length discussed in section 4, although for the dimensions of our system, a uniform distribution might be appropriate. It is, however, not of critical importance in this report because the observation points for which the fields are computed are located in the range $D >> D_0$, where the filament approximation can be used.

A rigorous prediction of the surface current distribution on the armature is not easy to obtain. To a first approximation one might assume that its vertical distribution is the same as that of the rails. Here again, if $D >> D_0$, the current filament approximation for the armature can also be used. For future EMC studies, where the determination of close-in magnetic fields may be important for implementing shielding, it is desirable to have available an analytical expression for the fields due to uniform sheet models. In this way one can obtain a first-order approximation of the importance of vertically distributed current sheets.

Figure 10. Geometry for computation of magnetic field contribution from armature.

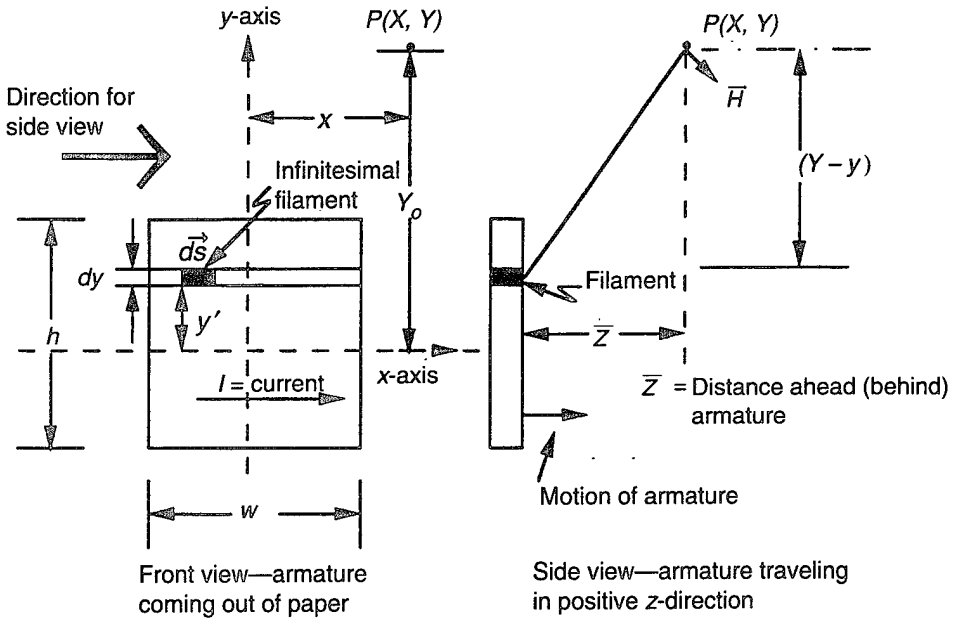

Figure 11. Geometry for computation of magnetic field contribution from rails.

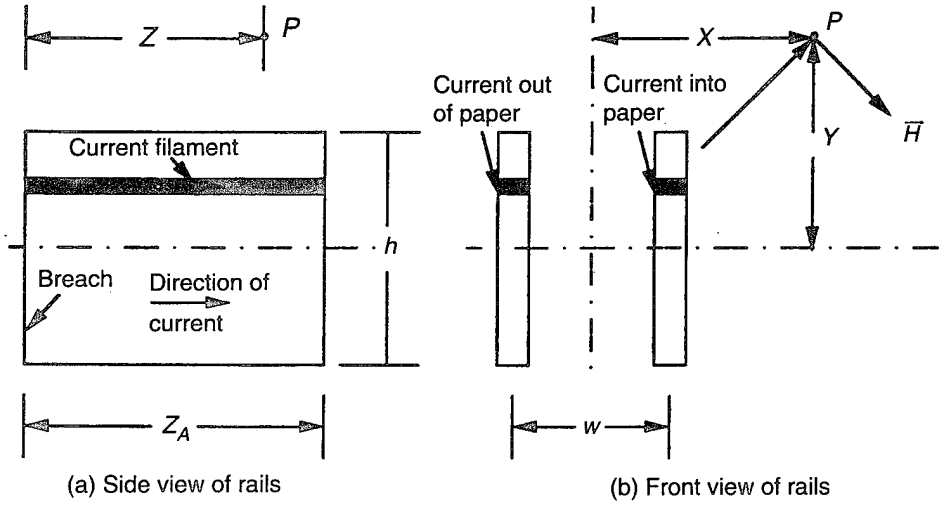

The z-component of $\vec{H}$ due to the armature is denoted as H_{Az}, and the y-component as H_{Ay}. These contributions are obtained by integrating equation (30) over the armature surface. Equivalent expression for the rails can be obtained with appropriate change of coordinates, but for brevity these results are not presented. For the sheet of uniform current density, J, we have

$$H_{Az} = \frac{J}{4\pi}[\alpha^+ G(\alpha^+) - \alpha^- G(\alpha^-)] \tag{30a}$$

$$H_{Ay} = -\frac{J}{4\pi}\overline{Z}[\alpha^+ N(\alpha^+) - \alpha^- N(\alpha^-)]\ , \tag{30b}$$

where

$$\alpha^+ = x + w/2 \ , \tag{30c}$$

$$\alpha^- = x - w/2 \ , \tag{30d}$$

$$G(\alpha) = \frac{1}{2\sqrt{\alpha^2}} \ln \frac{M_1}{M_2} \ , \tag{30e}$$

$$M_1 = \frac{R^+ - \sqrt{\alpha^2}}{R^+ + \sqrt{\alpha^2}} \ , \tag{30f}$$

$$M_2 = \frac{R^- - \sqrt{\alpha^2}}{R^- + \sqrt{\alpha^2}} \ , \tag{30g}$$

$$R^+ = \sqrt{\alpha^2 + \bar{Z}^2 + (Y + h/2)^2} \ , \tag{30h}$$

$$R^- = \sqrt{\alpha^2 + \bar{Z}^2 + (Y - h/2)^2} \ , \tag{30i}$$

$$N(\alpha) = \frac{1}{\sqrt{\alpha^2 \bar{Z}^2}} [\beta^+ - \beta^-] \ , \tag{30j}$$

$$\beta^+ = \arctan\left(\sqrt{\frac{\alpha^2}{\bar{Z}^2}} \frac{Y + h/2}{R^+} \right) , \tag{30k}$$

$$\beta^- = \arctan\left(\sqrt{\frac{\alpha^2}{\bar{Z}^2}} \frac{Y - h/2}{R^-} \right) \tag{30l}$$

$$\bar{Z} = Z - Z_A \ . \tag{30m}$$

When X or Y are much greater than w and h, the foregoing results reduce to the current filament approximation, with the total current given by Jh. We then have

$$H_{Az} = \frac{y}{4\pi} IK^* \ , \tag{31a}$$

$$H_{Ay} = \frac{-\bar{Z}}{4\pi} IK^* \ , \tag{31b}$$

where

$$K^* = \frac{1}{a_0^2} \left[\frac{(X + w/2)}{\left((X + w/2)^2 + a_0^2\right)^{1/2}} - \frac{(X - w/2)}{\left((X - w/2)^2 + a_0^2\right)^{1/2}} \right] , \tag{31c}$$

$$a_0^2 = \bar{Z}^2 + Y^2 \ . \tag{31d}$$

The magnetic fields due to the rails are H_{Rx} and H_{Ry}, and are given by

$$H_{Rx} = \frac{IY}{4\pi}(K_R - \bar{K}_R) \ , \tag{32a}$$

$$H_{Ry} = -\frac{I}{4\pi}[(X - w/2)\, K_R - (X + w/2)\, \bar{K}_R] \ , \tag{32b}$$

where

$$K_R = \frac{1}{b^2}\left[\frac{Z}{\left(Z^2 + b^2\right)^{1/2}} - \frac{\bar{Z}}{\left(\bar{Z}^2 + b^2\right)^{1/2}}\right] , \tag{32c}$$

$$b^2 = (X - w/2)^2 + Y^2 \ , \tag{32d}$$

$$\bar{K}_R = \frac{1}{\bar{b}^2}\left[\frac{Z}{\left(Z^2 + \bar{b}^2\right)^{1/2}} - \frac{\bar{Z}}{\left(\bar{Z}^2 + \bar{b}^2\right)^{1/2}}\right] , \tag{32e}$$

$$\bar{b}^2 = (X + w/2)^2 + Y^2 \ . \tag{32f}$$

6. Comparison Between Theory and Experiment

The primary emphasis of our study to date has been on the validation of the electromagnetic efficiency factor and the magnetic fields generated by the rail gun systems. The acceleration of the armature is given by equation (3). Using a measured current that has the waveform

$$I_0 = 190 \times 10^3 \left(\exp(-500\,t) - \exp(-1.3 \times 10^4\,t)\right) \quad (A)\ , \qquad (33)$$

we can immediately integrate equation (3) to obtain the velocity and position of the armature as a function of time. Figure 12 shows a representative comparison between the theoretical and experimental behavior of $Z_A(t)$ using equation (33) with an 11-g mass, and a theoretically predicted value of $L'_e = 0.39\ \mu H/m$. As observed, the agreement is good. The corresponding curve for velocity, $\dot{Z}_A(t)$, is also in good agreement with experimental results, yielding only a 7-percent uncertainty at the muzzle.

Figure 13 shows a comparison between the experimental and theoretical behavior of the vertical component of the magnetic field in the plane of symmetry at 2 in. above the rails and 28 in. from the breech. The theoretical result was obtained using equations (31), (32), and (33) and the time behavior of $Z_A(t)$ determined from the solution of equation (3). Although the comparison is good, we are still exploring the possible sources of error.

It is also interesting to observe the space-time variability of the magnetic field as a function of position. A sample result is shown in figure 14, for which all field components are indicated at the point z = 28 in., y = 4 in., and x = 0, 12, and 24 in., respectively. The observations are in general agreement with these results, although it is found that as we move away from the rails the experimental values begin to exceed the theoretical predictions by more than a factor of 2. We are exploring this matter further.

When the value $L' = E_0 L'_R = 0.39\ \mu H/m$ is used, the position of the armature, as determined by the peaking characteristic of the magnetic field reported in the forward (z-direction), is also consistent with experimental observations [1, 2]. This is shown in figure 15, where theoretical predictions of H_x, H_y, and H_z using a filament model for the rails and armature are rendered for z = 32 in., x = 0, and y = 12 in. The predicted time-to-peak of t_p = 2.4 ms for H_z lies within experimental uncertainty.

The experimental plot of H_z for the aforementioned case [1] has the same waveshape as that shown in figure 15 but is a factor of 2.5 higher. On the other hand, for observation points that are close to the rail there is very good agreement between the predicted and observed waveshapes and peak fields for all magnetic field components, with uncertainties approaching only 30 percent.

Appendix C provides a more comprehensive evaluation of calculated magnetic fields.

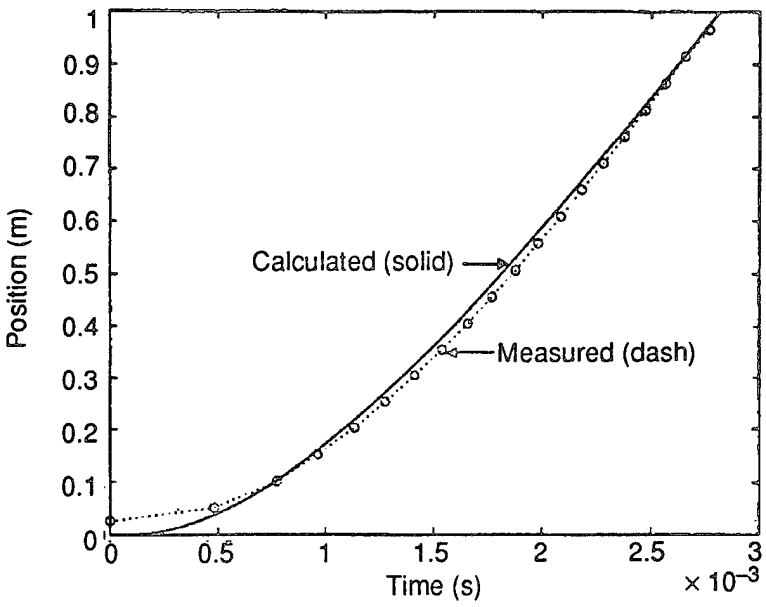

Figure 12. Armature position as a function of time. (Experiment results obtained from W.O. Coburn, ARL.)

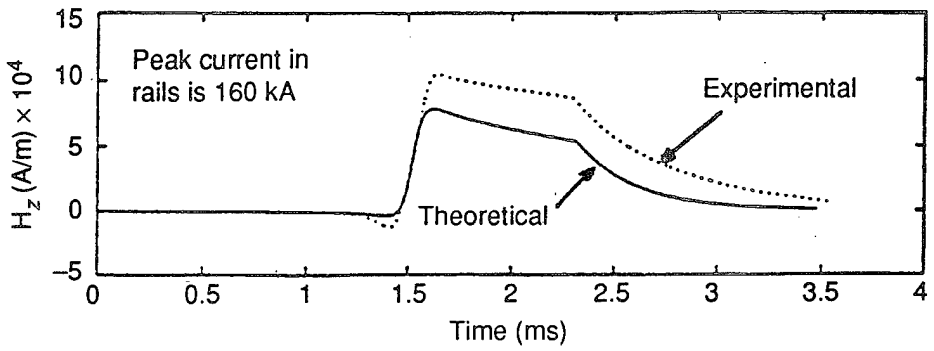

Figure 13. Comparison between experimental and theoretical behavior of vertical component of magnetic field in plane of symmetry at 2 in. above rails and 28 in. from breech. (Experimental results obtained from W. O. Coburn, ARL.)

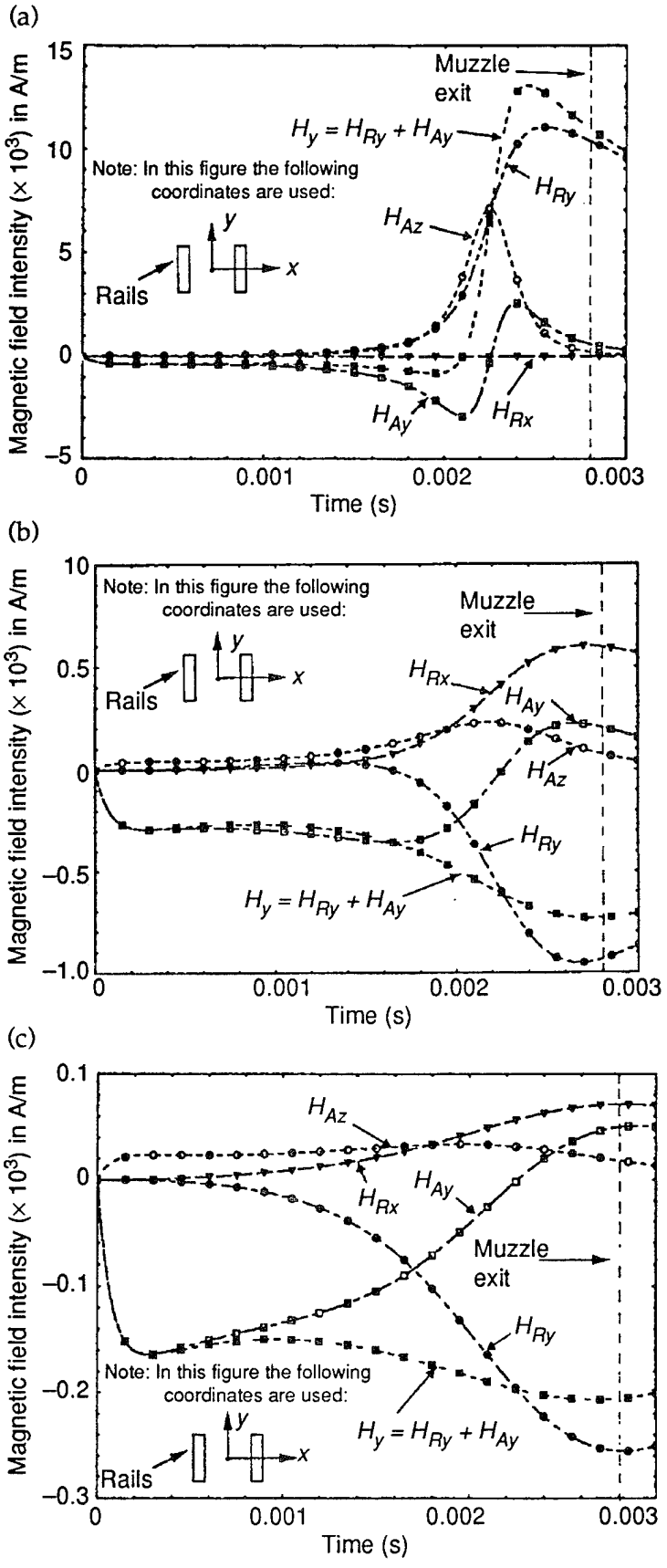

Figure 14. Magnetic field behavior at z = 28 in., y = 4 in., and (a) x = 0, (b) x = 12, and (c) x = 24 in.

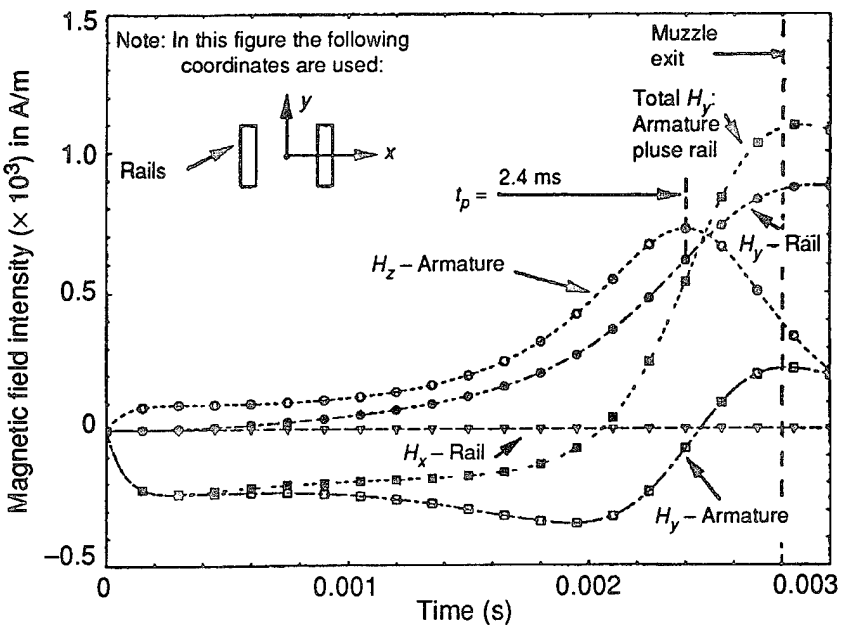

Figure 15. Armature and rail contributions to magnetic field intensity, H(A/m), z = 30 in. from breech, at height y = 12 in. above rails, and in plane of symmetry (x = 0). (Experimental results obtained from W. O. Coburn, ARL).

7. Conclusion

Predictions for projectile acceleration are in good agreement with experimental observations for rail gun inductance and efficiency factor. Muzzle exit velocity is found to be within 5 to 7 percent of experimental data. A comparison between calculated and measured magnetic fields shows good agreement close to the rails, with uncertainties exceeding a factor of two at large distances. These sources of error are being examined.

The large magnetic fields produced by these devices will require shielding in order to ensure compatability with other electronic equipment. Shielding considerations must be considered as an integral part of the rail gun design because it has a direct effect on the effective inductance for acceleration. This in turn influences size of the system and terminal projectile velocity.

Acknowledgement

The author wishes to thank William O. Coburn of the Army Research Laboratory for many helpful technical discussions and Paul Elliot for computer programming the time behavior of the magnetic fields.

References

1. W. O. Coburn, C. Le, D. DeTroye, G. Blair, and W. Williams, "Electromagnetic Field Measurements Near a Rail Gun," IEEE Trans. Magn. 30, No. 1, January 1995.

2. W. O. Coburn and W. Williams, "Static and Quasi-static Models for the Electromagnetic Environment of a Rail Gun," IEEE Trans. Magn. 30, No. 1, January 1995.

3. F. Assadourian and F. Rimai, "Simplified Theory of Microstrip Transmission Systems," Proc. IRE, 40: 1651, 1952.

4. C. E. Baum, "Impedances and Field Distributions for Parallel Plate Transmission Line Simulators," Sensor and Simulation Note 21, June 1966.

5. T. L. Brown and K. D. Granzow, "A Parameter Study of Two Parallel Plate Transmission Line Simulators of EMP," Sensor and Simulation Note 52, April 1968.

6. C. E. Baum, D. V. Giri, and R. D. Gonzalez, "Electromagnetic Field Distribution of the TEM Mode in a Symmetrical Two-Parallel-Plate Transmission Line," Sensor and Simulation Note 219, April 1976.

7. Moon and Spencer, *Field Theory Handbook*, Springer, 1961.

8. W. R. Smythe, *Static and Dynamic Electricity*, McGraw-Hill Book Company, New York, 1939.

9. A. Nussbaum, *Electromagnetic Theory for Engineers and Scientists*, Prentice-Hall, Inc., Englewood Cliffs, New Jersey, 1965.

10. G. F. Carrier, M. Krook, and C. E. Pearson, *Functions of a Complex Variable*, McGraw-Hill Book Company, New York, 1966.

11. R. E. Collin, *Foundations for Microwave Engineering*, McGraw-Hill Book Company, New York, 1992.

Appendix A.—Application of Transmission Line Theory to Rail Gun

This appendix discusses the importance of using a rigorous transmission line theory to provide an accurate representation of the electromagnetic fields in the spatial region around the rails. There are two reasons for executing this calculation. It will provide an improved evaluation of the electromagnetic efficiency

$$E_0 = \frac{\int_{-a}^{+a}\int_{-b}^{+b} H^2 dx\, dy}{\int_{-a}^{+a}\int_{-b}^{+b} H^2 dx\, dy + \int'\int' H^2 dx\, dy}, \qquad \text{(A-1)}$$

and may also provide insight into the coupling problems involving close-in shielding.

As we can see from equation (A-1) the determination of E_0 involves integration over the leakage volume $\int'\int'$. The question is how far from the rail bore center do significant contributions from $\int'\int' H^2\, dx\, dy$ exist? An estimate of this is available from the early work of Assadourian and Rimai [3], which is shown in figure A-1. This figure shows that virtually 100 percent of the power is contained over spatial dimensions that are of the order of the rail height. Although the calculations were performed using a value of $(b/a) = 0.86$ (which differs from the ARL value of $(b/a) = 0.80$), the results are not very different, as shown in figure 8.

Another important physical attribute of the rail gun system is the relatively large physical thickness of the rails as compared to the separation between them. Assadourian and Rimai [3] also provided an estimate of this effect which did not, however, appear to introduce important modifications to our conclusions. In a more refined calculation this aspect of the problem should be more critically addressed. Figure A-2 shows a comparison in the field lines between a thin and thick strip above a perfectly conducting plane.

In addition to references 3–7 (in the main body of text), the author has reviewed other conformal mapping approaches to the parallel plate transmission line system [9–11]. The important issue is to select the appropriate transformations in the complex to simplify the computation of E_0. Although some work has already been started in this arena, the results are too premature to present in this report.

In summary, a rigorous calculation (e.g., conformal mapping theory) is required to predict the fields in the close-in region surrounding the rails, and to determine the electromagnetic efficiency, E_0. The detailed structure of the currents on the rails would appear to be an important consideration in the fields for distances on the order of several rail heights. At larger distances from the bore center the filament approximation should suffice.

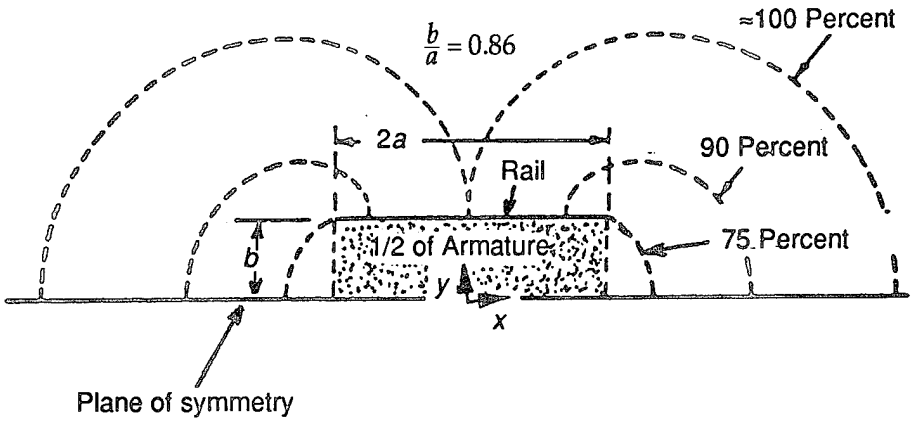

Figure A-1. Distribution of power flow for a wide strip of zero thickness above an infinite ground plane. (Figure source: ref. 3.)

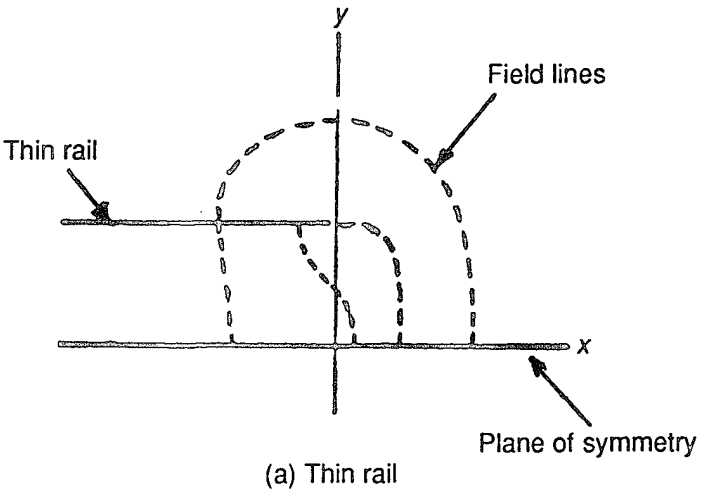

(a) Thin rail

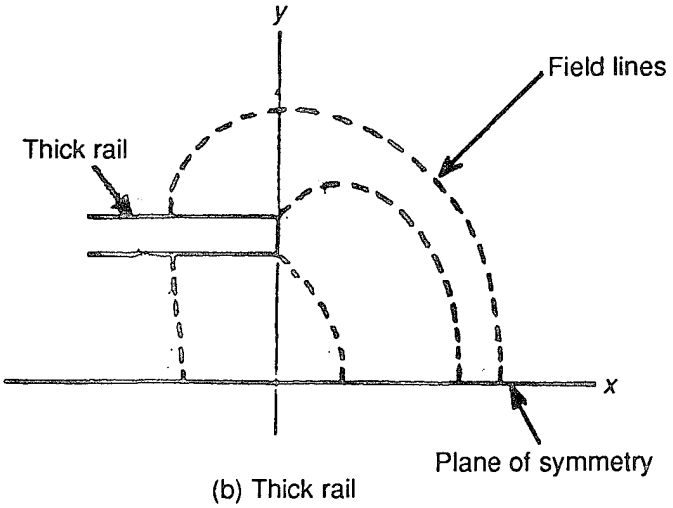

(b) Thick rail

Figure A-2. Comparison of field lines for thin and thick strips. (Figure source: ref. 3.)

Appendix B.—Equivalence Between Electric and Magnetic Fields in Two Dimensions

The theory of conformal mapping plays an important role in determining the spatial behavior of electric and magnetic fields in two dimensions. Traditionally, theoretical models are set up as electrostatic problems in which expressions for the electric fields follow directly. This appendix shows how the electrostatic results can be easily used to compute the spatial distribution of the magnetic fields when waves are propagated in the transmission line mode.

The existence of the aforementioned relationship has been pointed out to this author by Dr. Kelvin Lee,* although the derivation of the result was not available. Presumably, this result appears in the open literature. The equivalence formula between $\vec{H}$ and $\vec{E}$ presented here is independently derived, although the result is not new.

Consider the cross section for an arbitrarily shaped conducting surface shown in figure B-1. Current and charge are assumed to flow in the z-direction, which in this diagram is coming out of the paper. Let $q_s(\vec{\ell}, z)$ be the charge per unit area on the surface, and $j_s(\vec{\ell}, z)$ be the z-directed current per unit surface length. The differential charge located at position $\vec{\ell}$ on the surface is $q_s(\vec{\ell}, z)\, d\ell\, dz$ and the differential current is $j_s(\vec{\ell}, z)\, d\ell$, where $d\ell$ is the magnitude of $d\vec{\ell}$.

Now let $P(x, y, z)$ be any point exterior to the conductor as shown, which does not necessarily lie in the plane of the conducting surface element $d\ell\, dz$. The electric and magnetic fields at P due to the surface charge and current are respectively given by

$$\vec{E} = \frac{1}{4\pi\varepsilon_0}\int\int \frac{d\ell\, dz\vec{r}}{r^3} q_s(\vec{\ell}, z)\ , \tag{B-1}$$

$$\vec{B} = \frac{\mu_0}{4\pi}\int\int \frac{(\vec{k}\times\vec{r})\, d\ell\, dz}{r^3} j_s(\vec{\ell}, z)\ , \tag{B-2}$$

where $\vec{r}$ is the position vector from the surface element to P, $\vec{k}$ is a unit vector in the z-direction, and r is the magnitude of $\vec{r}$.

In the realm where the concepts of capacitance and inductance apply, which is the transmission line mode of propagation, the spatial distribu-

Private Communication, K. S. H. Lee, Kaman Sciences, Corp., Dikewood Division, Santa Monica, CA (September 1993).

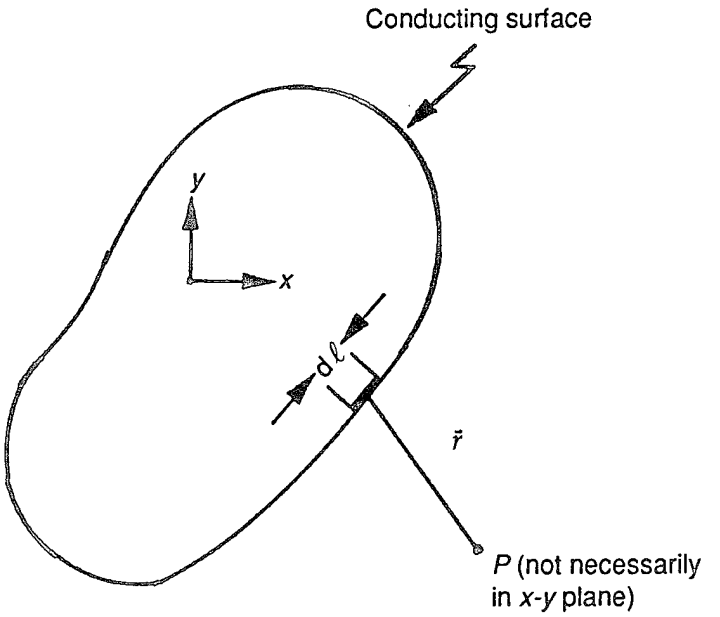

Figure B-1. Charge and current on conducting surface.

tions of surface charge and surface current are similar. We can therefore write

$$q_s(\vec{\ell}, z) = Q(z)\eta(\vec{\ell}, z) \ , \tag{B-3}$$

$$j_s(\vec{\ell}, z) = I(z)\eta(\vec{\ell}, z) \ , \tag{B-4}$$

where $Q(z)$ is the charge per unit length at position z, $I(z)$ is the current at z, and $\eta(\vec{\ell},z)$ is a normalized spatial distribution function that satisfies the condition

$$\int \eta(\vec{\ell}, z)\, d\ell = 1 \ . \tag{B-5}$$

The integration of equation (B-5) is completely around the conducting surface at fixed z.

When the conditions for conformal mapping apply, the spatial variations with z are neglected. Thus, Q, I, and η are no longer functions of z. In this domain we form the vector cross product, $\vec{k} \times \vec{E}$, using equation (B-1). The result is

$$\vec{k} \times \vec{E} = \frac{Q}{4\pi\varepsilon_0} \int \int \frac{\eta(\vec{\ell})\, dz\, d\ell}{r^3}\, \vec{k} \times \vec{r} \ . \tag{B-6}$$

Using equation (B-4) in equation (B-2) we deduce

$$\vec{B} = \frac{\mu_0 I}{4\pi} \int \int \frac{\eta(\vec{\ell})\, dz\, d\ell}{r^3}\, \vec{k} \times \vec{r} \ . \tag{B-7}$$

By comparing equations (B-6) and (B-7) and using the formula $\vec{B} = \mu_0 \vec{H}$, we derive the desired result

$$\vec{H} = \frac{I}{Q} \varepsilon_0 \vec{k} \times \vec{E} \quad . \tag{B-8}$$

Equation (B-8) is used in conjunction with conformal mapping applied to electrostatics in the following way. Suppose the electrostatic problem is set in accordance with the discussion of section 4.2. The charge, Q, appearing on either rail, as well as the electric field, $\vec{E}$, are both proportional to the initially assigned arbitrary voltage, V_0. The ratio, $\vec{E}/Q$, is an intrinsic property of the system, that is, independent of V_0. By simply specifying a total current, I, flowing on either rail, we can readily determine the magnetic intensity, $\vec{H}$, from equation (B-8).

Appendix C .—Time Behavior of Magnetic Field at Selected Field Points

This appendix presents results for the magnetic field behavior at selected points to show the variability with distance along the rails (fig. C-1 to C-6), variability with height above the rails in the plane of symmetry (fig. C-7 to C-11), and the variability with displacement off the plane of symmetry (fig. C-8 and fig. C-12 to C-15). The legend in these figures is explained below.

In these figures the following coordinates are used:

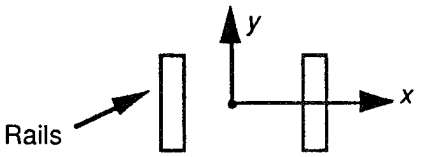

Used in text	Used in figures
H_{Ay}	AY
H_{Az}	AZ
H_{Ry}	RY
H_{Rx}	RX
$H_{Ay} + H_{Ry}$	$AY + RY$

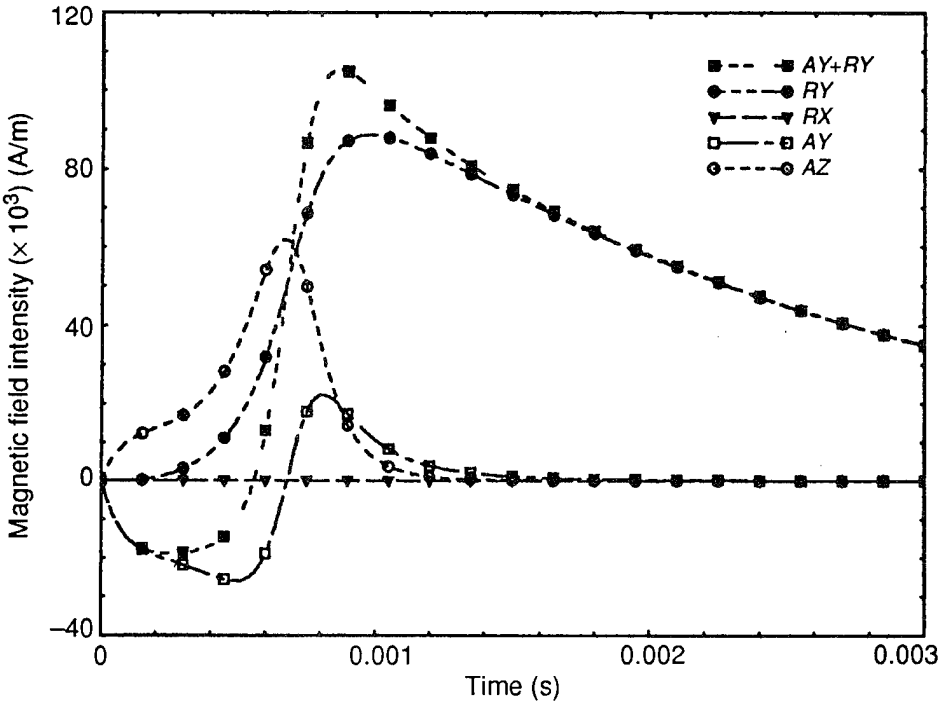

Figure C-1. Magnetic field behavior at $x = 0$ in., $y = 2$ in., and $z = 3$ in.

Figure C-2. Magnetic field behavior at x = 0, y = 2 in., and z = 20 in.

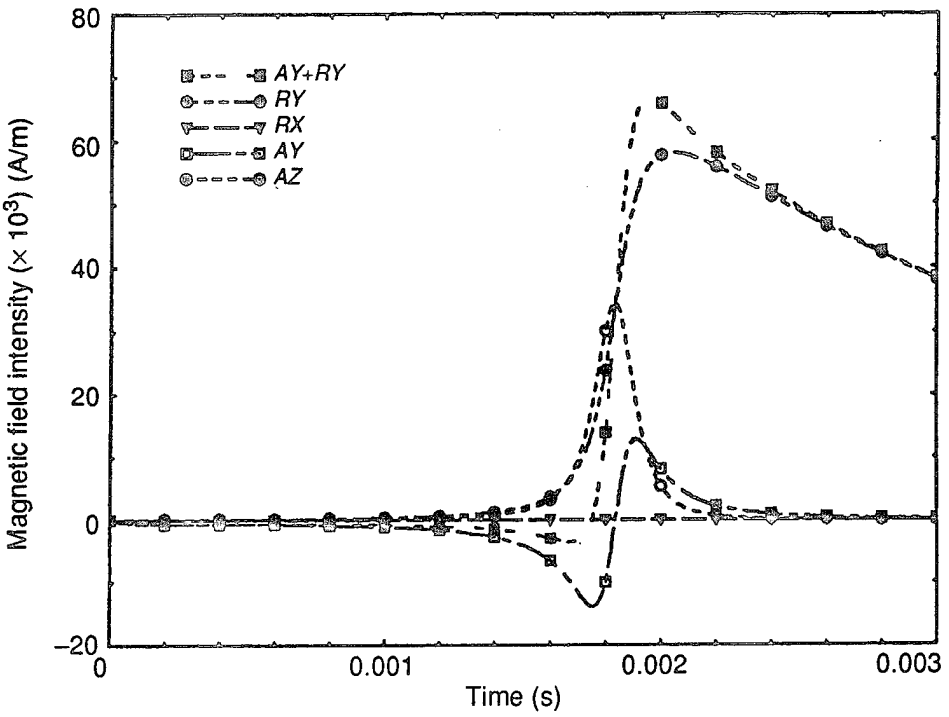

Figure C-3. Magnetic field behavior at x = 0, y = 4 in., and z = 30 in.

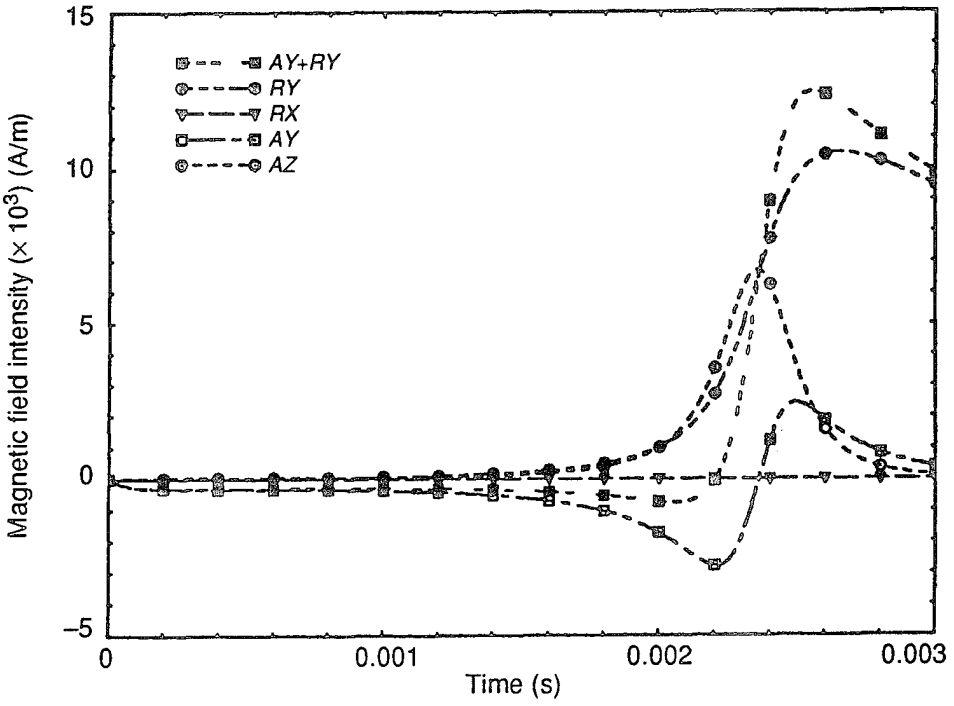

Figure C-4. Magnetic field behavior at $x = 0$, $y = 4$ in., and $z = 32$ in.

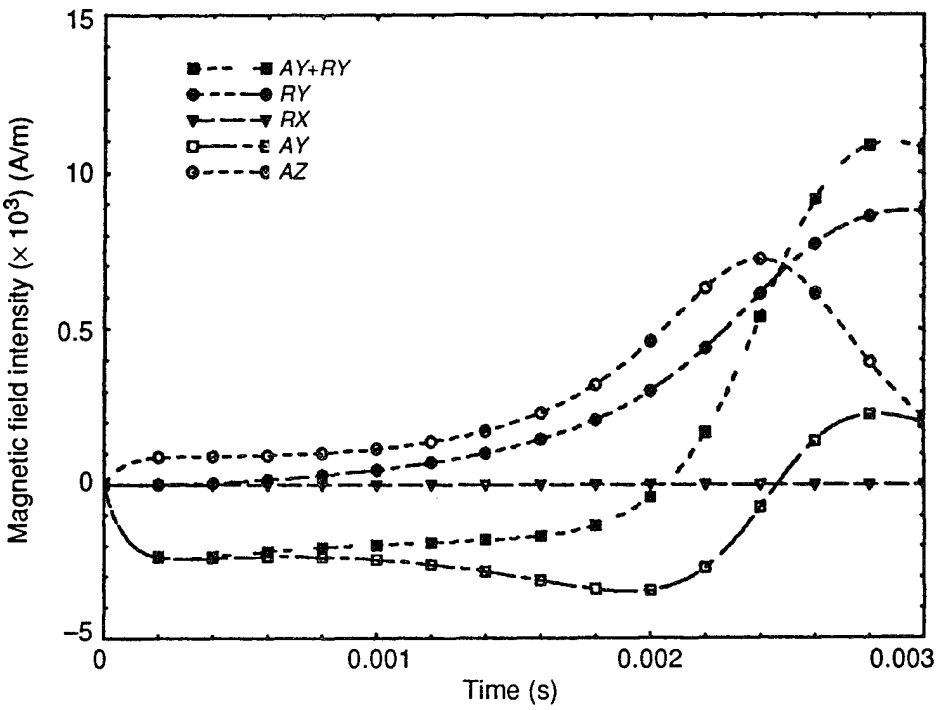

Figure C-5. Magnetic field behavior at $x = 0$, $y = 22$ in., and $z = 32$ in.

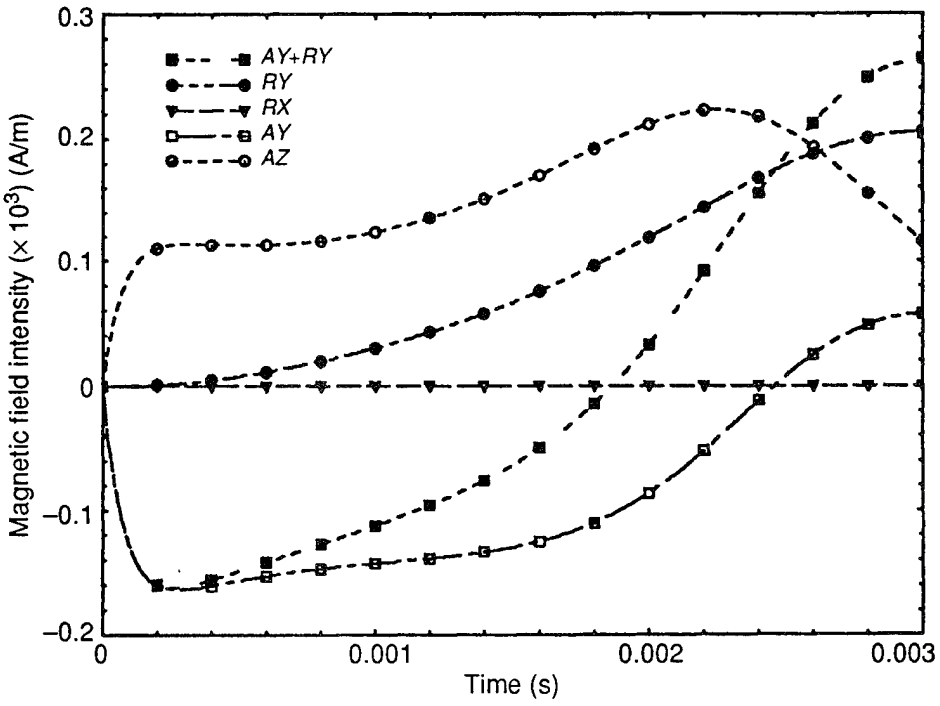

Figure C-6. Magnetic field behavior at $x = 0$, $y = 2$ in., and $z = 37$ in.

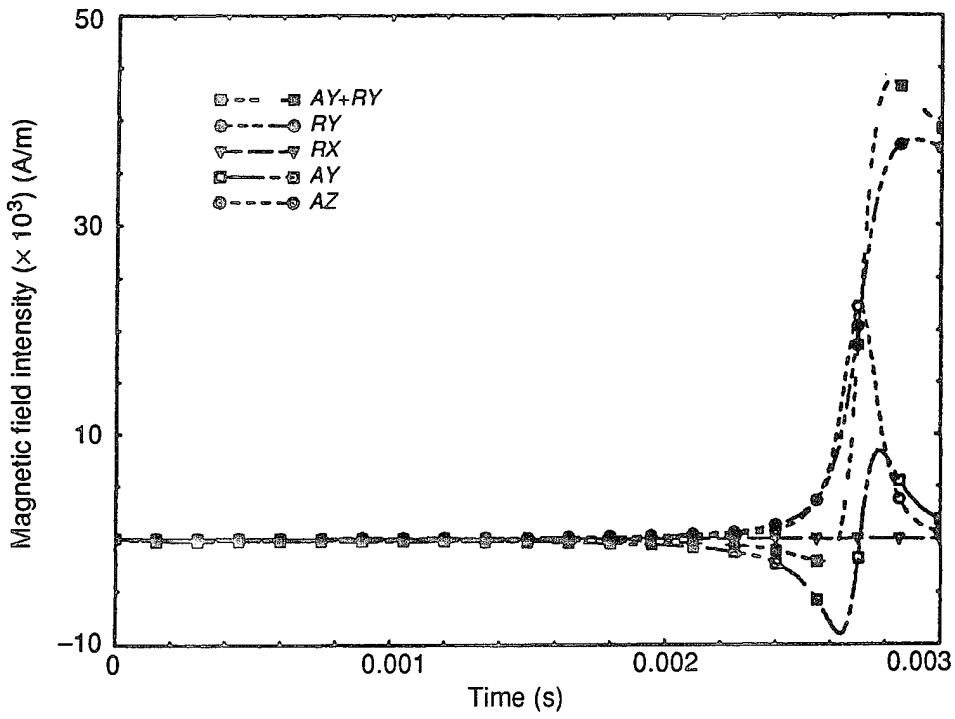

Figure C-7. Magnetic field behavior at $x = 0$, $y = 2$ in., and $z = 28$ in.

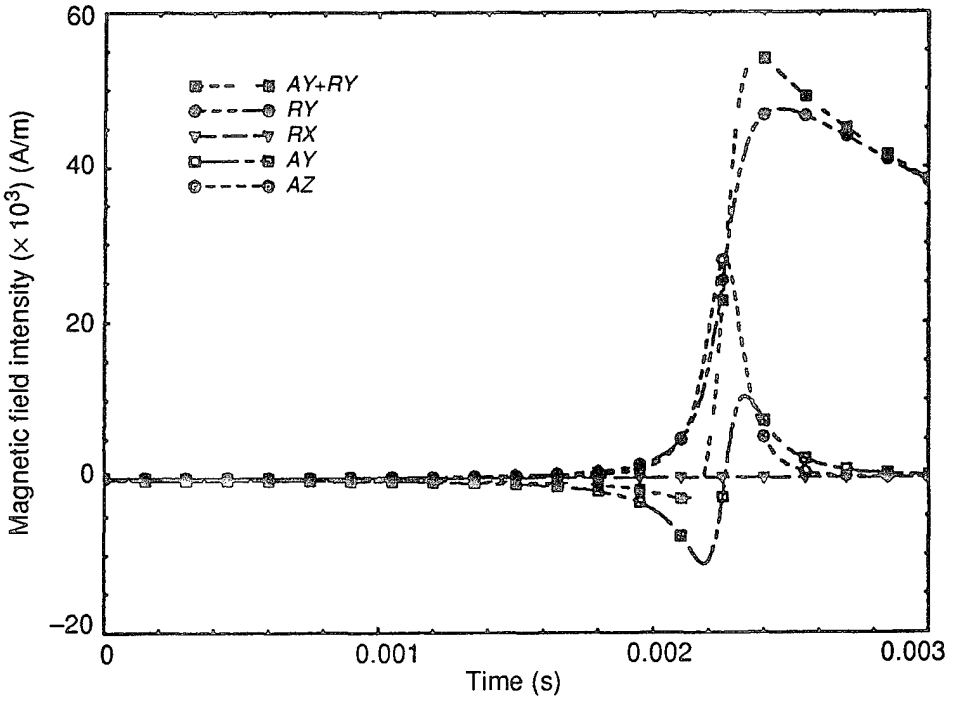

Figure C-8. Magnetic field behavior at x = 0, y = 4 in., and z = 28 in.

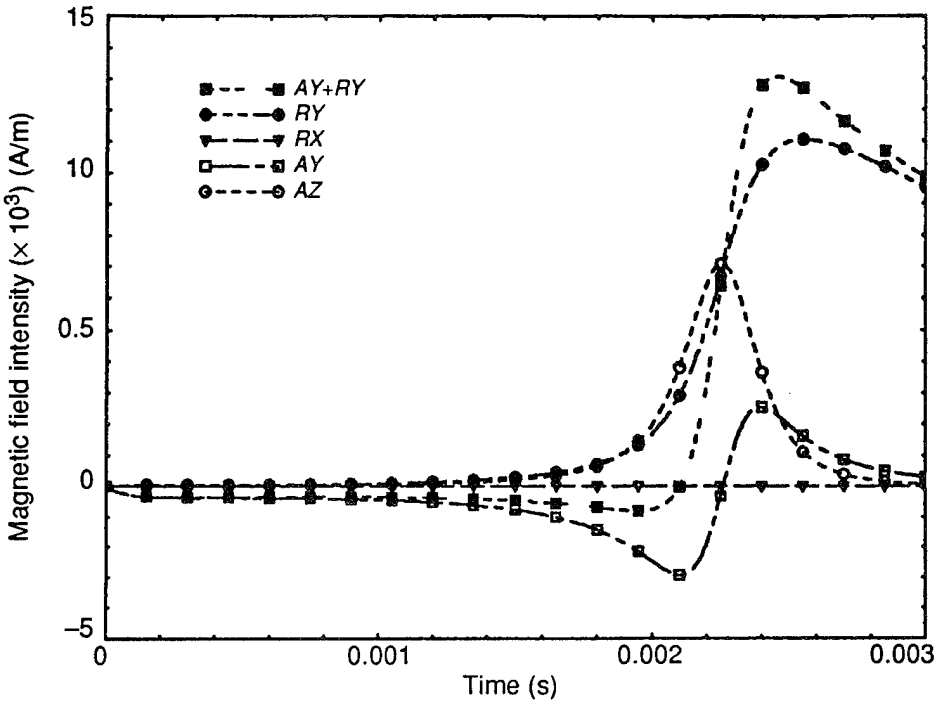

Figure C-9. Magnetic field behavior at x = 0, y = 8 in., and z = 28 in.

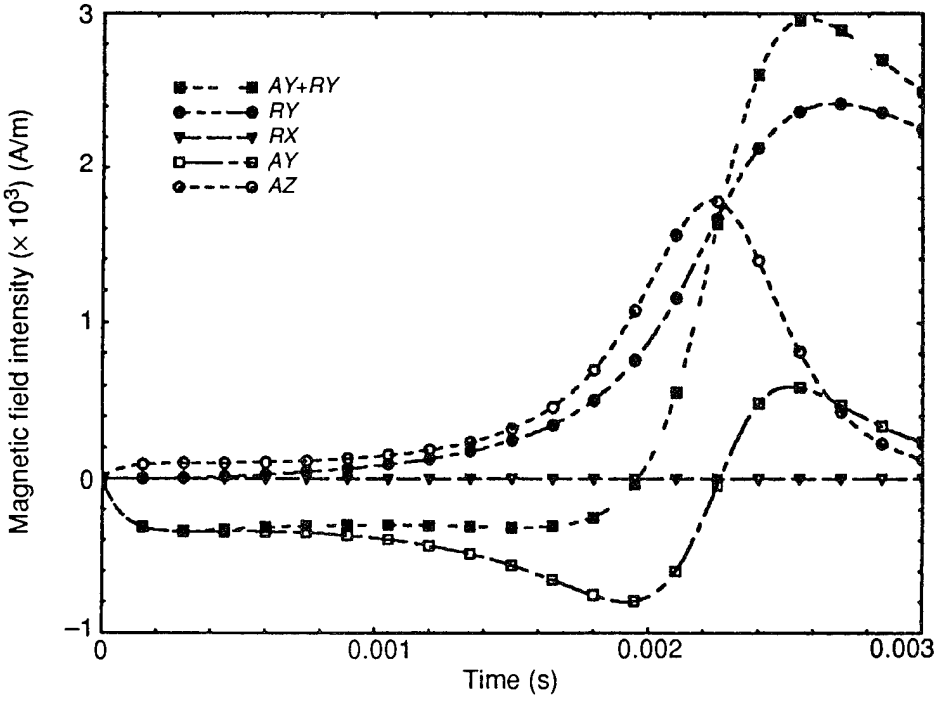

Figure C-10. Magnetic field behavior at $x = 0$, $y = 12$ in., and $z = 28$ in.

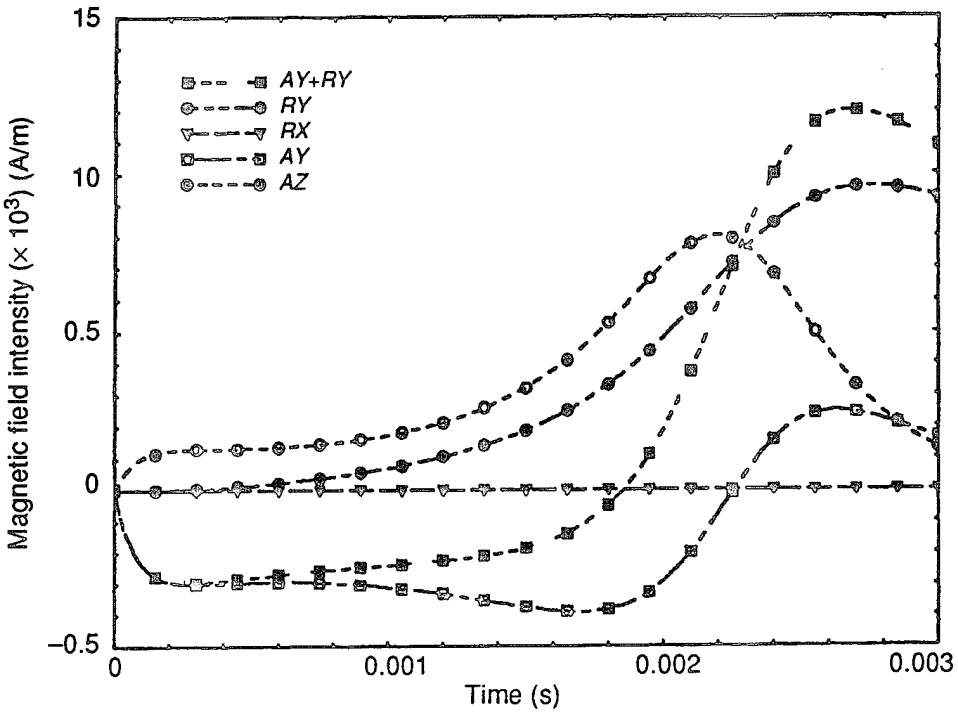

Figure C-11. Magnetic field behavior at $x = 0$, $y = 24$ in., and $z = 28$ in.

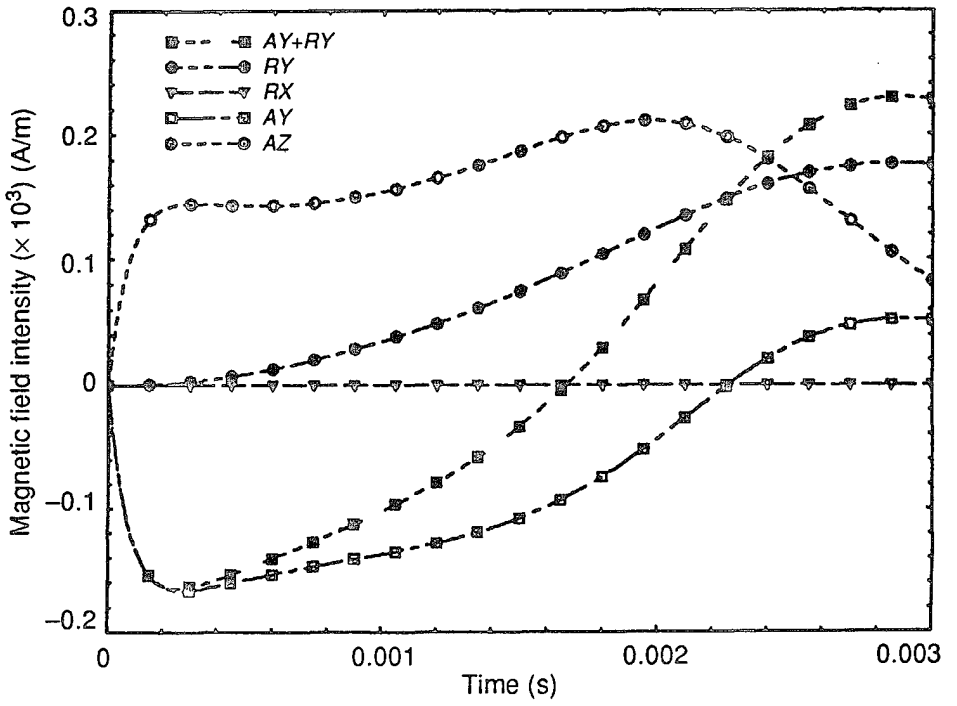

Figure C-12. Magnetic field behavior at $x = 2$ in., $y = 4$ in., and $z = 28$ in.

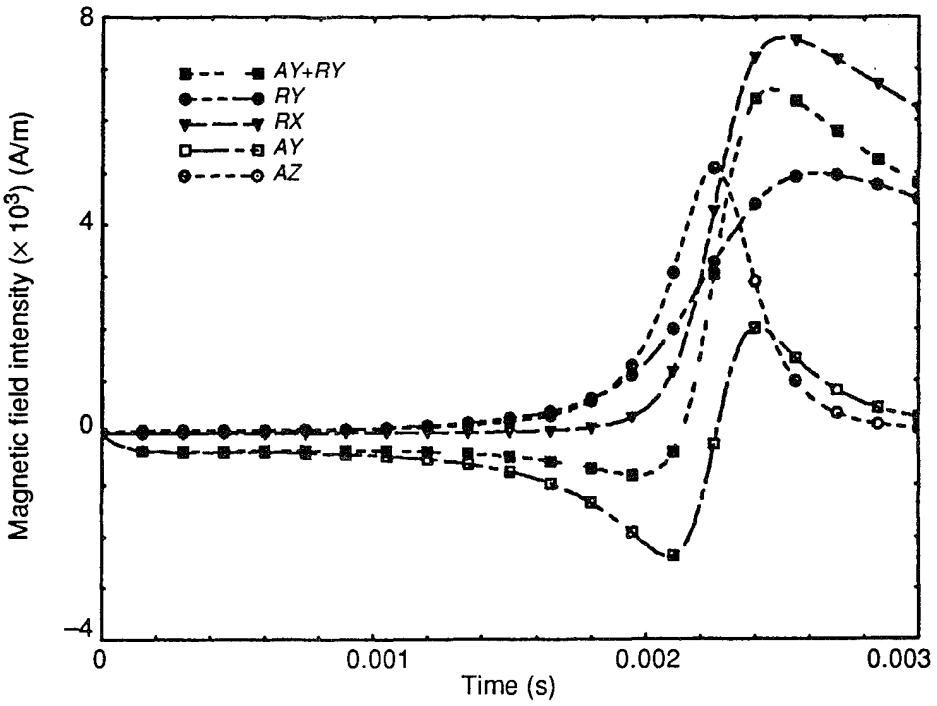

Figure C-13. Magnetic field behavior at $x = 4$ in., $y = 4$ in., and $z = 28$ in.

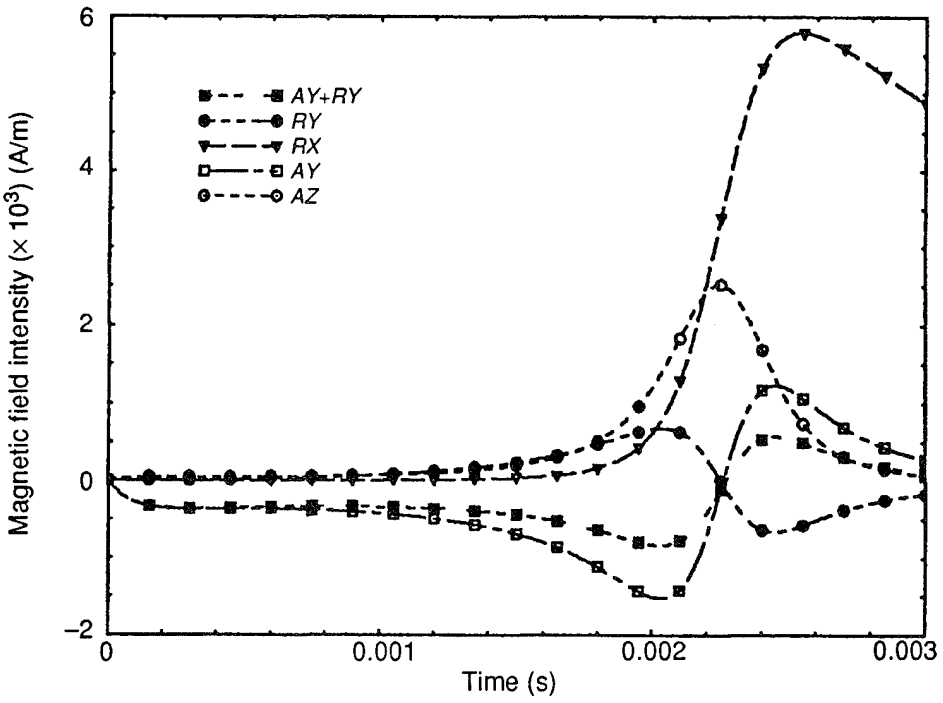

Figure C-14. Magnetic field behavior at $x = 12$ in., $y = 4$ in., and $z = 28$ in.

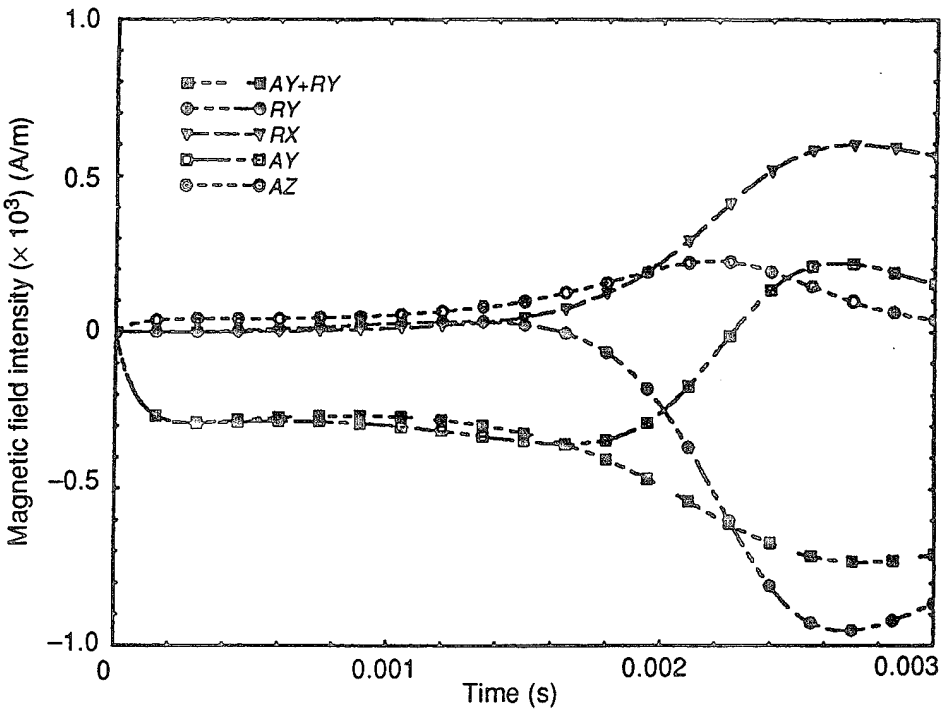

Figure C-15. Magnetic field behavior at $x = 24$ in., $y = 4$ in., and $z = 28$ in.

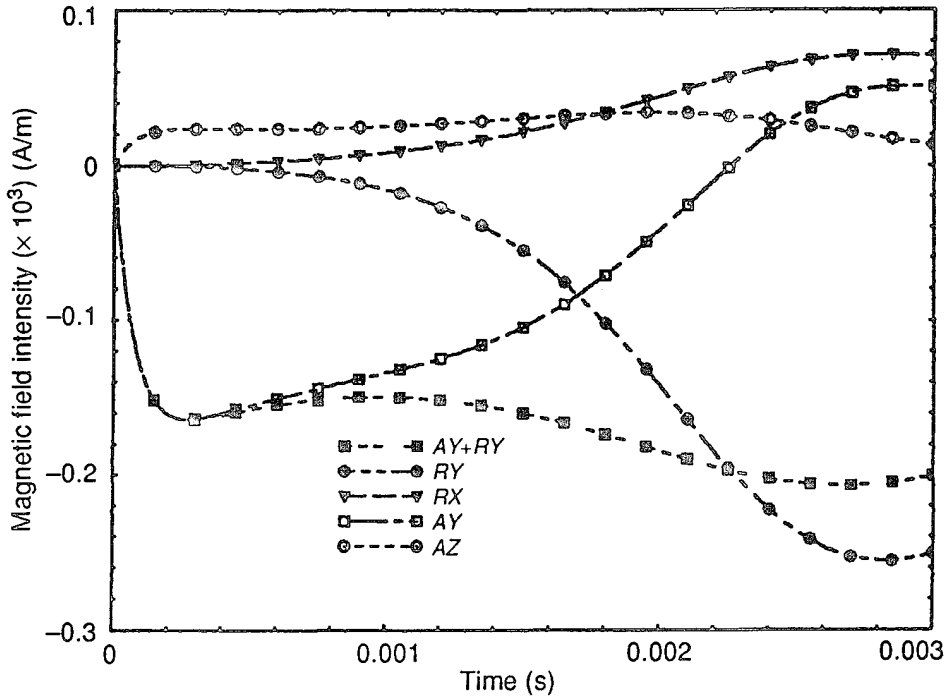

Distribution

Admnstr
Defns Techl Info Ctr
Attn DTIC-DDA (2 copies)
Cameron Sta Bldg 5
Alexandria VA 22304-6145

Defs Nuc Agency
Office of Techl Applications
Attn D R Lewis
6801 Telegraph Rd
Alexandria VA 22310

DoD Electromagnetic Compatibility Anlys Ctr
Attn CA J Word (3 copies)
120 Worthing Basin
Annapolis MD 21401

HQ TECOM
Attn AMSTE-TC-D B Bell
Aberdeen Proving Ground MD 21005-5055

Ofc of the Assist Secy of the Army for Rsrch
Dev & Acqstn
Attn SARD-TR R Chait
Room 3E476 The Pentagon
Washington DC 20310-0103

Cmdr
US Army ARDEC
Attn SMCAR-CCL-FA W Williams
(3 copies)
Bldg 65 N
Picatinny Arsenal NJ 07806-5000

US Army Natick RDEC
Attn SATNC-SUSD-SHD A Murphy
Attn SATNC-SUSD-SHD J Siegel
Kansas Street
Natick MA 01760-5018

Commander
US Army TACOM Nuclear Effects
Directorate
Attn STEWS-NE J Meason
White Sands Missile Range NM 88002-5180

US Military Academy
Dept of Elec Eng & Computer Sci
Attn CPT K Reinhard
West Point NY 10996

Dir Air Force Armament Directorate
Attn WL/MNAA S Federle
101 W Eglin Blvd Ste 346A
Eglin AFB FL 32542-6810

Nav Warfare Ctr
Attn Code 0ZT T Conway
Lakehurst NJ 08733

Univ of Texas at Austin
Ctr for Electromagnetics
Attn Code 77000 J Kitzmiller
Balcones Rsrch Ctr
Austin TX 78712

FMC Corp
Nav Systems Div
Attn B Anderson
4800 E River Rd
Minneapolis MN 55421

Kohlberg Associates, Inc
5375 Duke St Unit 1603 (10 copies)
Alexander VA 22304

US Army Rsrch Lab
Attn AMSRL-OP-SD-TA Mail & Records
Mgmt
Attn AMSRL-OP-SD-TL Tech Library
(3 copies)
Attn AMSRL-OP-SD-TP Tech Pub
Attn AMSRL-WT-ND W O Coburn
(5 copies)
Attn AMSRL-WT-ND C Le
(5 copies)
Attn AMSRL-WT-PB Chf
Attn AMSRL-WT-WB Chf
Attn AMSRL-WT-WD Chf